MIT Open Access Articles

3D Stereoscopic PIV visualization of the axisymmetric conical internal wave field generated by an oscillating sphere

Massachusetts Institute of Technology

3D Stereoscopic PIV visualization of the axisymmetric conical internal wave field generated by an oscillating sphere

Sasan John Saidi · Thomas Peacock

Abstract To date, experimental studies of internal wave velocity fields have been limited to two-dimensional investigations of planar or axisymmetric systems. Here we present results of the first three-dimensional stereoscopic PIV visualizations of an internal wave field. The experiments utilize the canonical arrangement of a vertically oscillating sphere, which enables rigorous comparison with recently published theoretical results. The excellent level of agreement between experiment and theory demonstrates the utility of using stereoscopic PIV to study three-dimensional internal waves. Furthermore, the ability to measure all three components of the velocity field gives an alternative perspective on the significance of harmonics generated via nonlinear processes in the vicinity of the oscillating sphere.

1 Introduction

Internal waves are propagating perturbations in a density-stratified fluid; the types of density stratifications in which they are manifest can range from a series of discrete layers of uniform density to a continuous, even nonlinear, variation of density with height. The latter is typical of the ocean and atmosphere, where internal waves are responsible for significant transport of energy and momentum, respectively (Garrett and Kunze, 2007).

The significance of internal waves is reflected in their extensive laboratory study, beginning with the work of Gortler (1943), who was the first to visualize internal waves using an early Schlieren technique, and to verify the dispersion relation. A more detailed survey of visualization techniques for stratified flows was offered by Mowbray (1967) who considered dye bands, shadowgraph and Schlieren methods; this lead to the celebrated studies of the St. Andrew's Cross by Mowbray and Rarity (1967).

A more readily quantifiable measurement system than the traditional Schlieren technique is the Synthetic Schlieren (SS) method developed by Sutherland et al. (1999). This has been the primary measurement tool for laboratory studies of internal waves over the past decade. SS has been extensively used to visualize two-dimensional (2D)

Department of Mechanical Engineering, Massachusetts Institute of Technology, Cambridge, MA 02139, USA

internal waves generated by oscillating bodies (Sutherland and Linden, 2002; Peacock et al., 2008) and wave beam propagation (Mercier et al., 2008; Mathur and Peacock, 2009), to name but a few examples. The SS method has also been adapted to investigate axisymmetric wave fields (Flynn et al., 2003; Yick et al., 2009). Most recently, Hazewinkel et al. (2011) investigated truly three-dimensional (3D) internal wave fields in a paraboloid by reconstructing the density field through the use of tomographic SS.

In the last decade, Particle Image Velocimetry (PIV) has become a widely accessible tool for laboratory studies of internal waves, although it is worth nothing that Thomas and Stevenson (1972) were perhaps first on the scene with their study of the motion of neutrally buoyant oil drops in an internal wave field. Employing the PIV technique, Zhang et al. (2007) studied internal wave generation using a horizontally oscillating cylinder to mimic ocean bottom topography, while Echeverri et al. (2009) analyzed the modal content of an internal wave field generated by a large amplitude ocean ridge. King et al. (2009) studied internal wave fields generated by an axisymmetric Gaussian ridge, though they were restricted to planar measurements in the planes coincident and perpendicular to the forcing direction.

A rich history accompanies the canonical arrangement of an oscillating sphere in a density stratified fluid, which has been the subject of extensive theoretical and experimental investigation and is the configuration considered in this paper. The recent work of Voisin et al. (2011) provides a comprehensive summary of these efforts, as well as presenting new theoretical and experimental results for an oscillating sphere. A fluorescent dye experimental technique was used rather than PIV from which they were able to derive velocity field data via displacement field data. Very good agreement between experiment and theory was obtained, although the dye-based method was inherently limited to the determination of only vertical velocity components.

To date, there has been no investigation of a 3D internal wave field using stereoscopic PIV. The configuration of a vertically oscillating sphere in a linearly stratified ambient provides an excellent scenario for first attempting this. The focus of this paper is to therefore use the stereoscopic PIV technique to rigorously test recent theoretical predictions for all three velocity components of the conical wave beams generated by an oscillating sphere. We proceed with a review of the associated theory in section 2, and a description of the experimental apparatus in section 3. An overview of the stereoscopic PIV arrangement is provided in section 4, and the results of the experiments are presented in section 5. Lastly, in section 6 we put forth concluding remarks.

2 Theory

Hurley (1972) developed an analytical method for solving steady-state propagation problems in two dimensions by initially focusing on the scenario $\omega > N$, where ω is the internal wave frequency and $N = \sqrt{-(g/\rho_o)\mathrm{d}\bar{\rho}/\mathrm{d}z}$ is the background buoyancy frequency of the stratification in the Boussinesq limit, ρ_o is a reference density value, $\bar{\rho}(z)$ is the background density stratification and g is gravity. He used conformal mapping to solve the elliptic boundary value problem, and then extended the solution for $\omega < N$ by analytic continuation. This work was furthered by Appleby and Crighton (1987) to obtain solutions for the oscillating sphere. The aforementioned solutions were all inviscid, a consequence of which is unboundedness of the solution along the lines defining the wave beam. Flynn et al. (2003) remedied the situation by adopting the boundary layer approximation of Thomas and Stevenson (1972) and the method of

Lighthill (1978) to derive an analytic solution to the viscous problem. A direct result of viscous attenuation is a bimodal-to-unimodal transition of the wave beam structure; these results were experimentally verified by Flynn et al. (2003).

Most recently, Voisin et al. (2011) developed a 3D formulation accounting for viscosity and transient effects in both the near and far field of an oscillating sphere. In this approach, the sphere is characterized by its radius R, oscillation amplitude A and frequency ω. Following Voisin et al. (2011), the expressions for the velocity components of the axisymmetric conical internal wave field in conventional cylindrical coordinates (x_r, x_z) are:

$$u_r(x_r, x_z) = \omega A \sin\theta\cos\theta \int_0^{\frac{R\sin\theta}{|x_z|\alpha}} \exp\left(\frac{-\beta k^3 |x_z|}{\sin\theta} - \mathrm{i}k|x_z|\cos\theta\right)$$
$$\times \frac{R^2 k \cos\theta}{1 - B(\sin\theta)}\, j_1(Rk)\, J_1(kx_r\sin\theta)\, \mathrm{d}k, \tag{1}$$

$$u_z(x_r, x_z) = \omega A \sin^2\theta \int_0^{\frac{R\sin\theta}{|x_z|\alpha}} \exp\left(\frac{-\beta k^3 |x_z|}{\sin\theta} - \mathrm{i}k|x_z|\cos\theta\right)$$
$$\times \frac{\mathrm{i}R^2 k \cos\theta}{1 - B(\sin\theta)}\, j_1(Rk)\, J_0(kx_r\sin\theta)\, \mathrm{d}k, \tag{2}$$

where

$$\alpha = (\omega t \tan\theta)^{-1}, \tag{3}$$

$$\beta = \nu/2\omega\tan\theta, \tag{4}$$

$$B(\sin\theta) = \sin^2\theta\left[1 - \cos\theta\left(\operatorname{arctanh}(\cos\theta) + \frac{\mathrm{i}\pi}{2}\right)\right], \tag{5}$$

k is the wavenumber, ν is the kinematic viscosity of the fluid, $\theta = \sin^{-1}(\omega/N)$ is the angle the wave cones make with the horizontal and

$$j_n(x) = \sqrt{\frac{\pi}{2x}} J_{n+\frac{1}{2}}(x) \tag{6}$$

is the relation between the spherical Bessel function j_n and the cylindrical Bessel function J_n. In evaluating the integrals in Eqs. 1 and 2 we select both a sufficiently large upper limit and a fine enough discretization for k such that the integral converges. Further details of this approach and the formulation of the boundary integral problem are provided by Voisin (2003).

Figure 1 shows the expected conical wave beam structure and the coordinate systems employed by the analysis. To recover the theoretical solutions in the Cartesian frame the following transformation is used:

$$\begin{bmatrix} u \\ v \\ w \end{bmatrix} = \begin{bmatrix} \sin\phi & 0 \\ \cos\phi & 0 \\ 0 & 1 \end{bmatrix} \begin{bmatrix} u_r \\ u_z \end{bmatrix} \tag{7}$$

where $\phi = \arctan(-x/y)$. Time dependency is introduced via $\mathbf{U} = \operatorname{Re}\left[(u, v, w)\exp(-\mathrm{i}\omega t)\right]$ to produce the final form of the solution. For the purpose of presenting our results within any x, z-plane we use a coordinate system (s, σ) that is aligned with the downward propagating wave structure captured in a cross-sectional plane. The coordinates (x, z) and (s, σ) are related by:

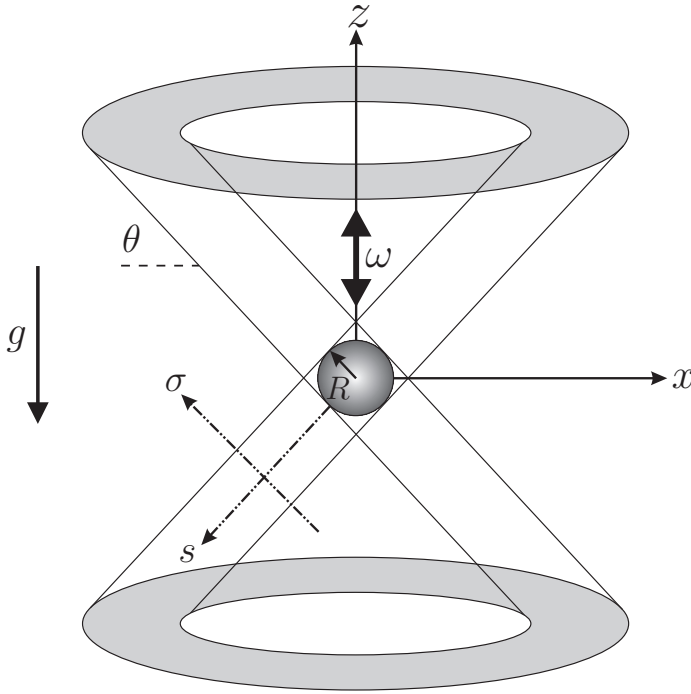$$s = -x\cos\theta - z\sin\theta, \tag{8}$$

Fig. 1 Wave cone structure for a sphere oscillating vertically at forcing frequency ω. For the experiments described in this paper we resolve the wave field in quadrant 3, this being the lower left hand quadrant $(x, z < 0)$. The coordinate system for this quadrant (s, σ) has ordinates that are tangential and perpendicular, respectively, to the wave cone. The y coordinate is into the page and is the same for the (x, z) and (s, σ) coordinate systems employed.

$$\sigma = -x \sin \theta + z \cos \theta, \tag{9}$$

with y being a common coordinate between the two systems.

3 Experimental set-up

Experiments were performed in an acrylic tank measuring 55 cm wide, 75 cm long and 40 cm tall. A linear salt-stratification over 38 cm depth was set up in the tank using the double bucket method (Oster and Yamamoto, 1963). The tank was stratified from below using two Masterflex peristaltic pumps with flow rates set at 0.5 and 0.25 liters/min. The resulting density stratification, measured using a calibrated PME salinity probe attached to a linear traverse for position control, was highly linear. Using a linear fit to find the density profile the experimental value of N was $N = 0.870 \pm 0.004$ rad/s. The kinematic viscosity of the saline water was measured to be $\nu = 1 \pm 0.01$ mm^2/s.

A schematic of the experimental arrangement is presented in Fig. 2. The region of study for visualization was quadrant 3 $(x, z < 0)$ of the (x, z) Cartesian coordinate system centered on the resting position of the sphere, which was suspended 24 cm above the tank bottom. Prior to filling, the sphere was positioned in the tank such that quadrant 3 was adequately covered by the field of view of the two cameras for the stereoscopic set-up. Tests were run to confirm the axisymmetric nature of the wave

field, making the decision to focus on a single quadrant quite reasonable. The sphere, which was of diameter $2R = 53.9$ mm, was affixed to the end of a thin rod of diameter 8 mm, which in turn was connected to a linear traverse controlled via LabView software. The trajectory of the sphere underwent a ramped, vertical oscillatory motion which took 7 periods to reach the maximum amplitude of $A = 5.0 \pm 0.05$ mm. To mitigate wave reflections Blocksom matting (a rough, finely interwoven, laminated coconut hair matting) was placed on a majority of the interior bottom and side walls of the tank. The experimental data used in our analysis covered several (4-6) time periods for the time window after the wave field first achieved a harmonic state (after ~ 9 periods) and before any reflections entered the field of view. Plastic wrap was placed over the top of the tank to prevent convection driven by evaporation and ambient air circulation.

Based on the dispersion relation, $\sin \theta = \omega/N$, the propagation angle of internal waves is directly controlled by setting the frequency of oscillation. In this study, we observed wave cones propagating at angles of $\theta = 20.3°$ and $38.2°$ (to within an error of $\pm 0.5°$), the corresponding Reynolds numbers ($Re = 2\omega R^2/\nu$) for these experiments being $Re \simeq 440$ and 780, respectively. The axisymmetric wave cones were visualized at three vertical cross-sections: the first cross-section cut through the center of the sphere in the plane $y = 0.0$ cm, while the other two visualization planes were at $y = -4.0$ and $y = -8.0$ cm (to within an error of ± 2 mm). Black contact paper was affixed to the external tank walls to minimize laser reflection. When imaging the cross-section at $y = 0$ cm, laser light scattering from the sphere was observed, so we placed additional tape over appropriate areas of the tank front wall to prevent damage to the CCD cameras.

4 Stereoscopic PIV arrangement

The salt-stratified water was seeded with SPHERICEL hollow glass oxide particles having a mean diameter of $8 - 12 \, \mu$m and a specific gravity between $0.1 - 1.5$, which covered the density range of the stratification. The particles were evenly mixed within the double bucket system and left to settle to their respective density levels for four hours after filling. The entire stratification was observed to contain sufficient amounts of seeding throughout for high-quality visualization.

A pulsed Nd:YAG laser passed through a diverging cylindrical lens was used to create the light sheet that illuminated the particles in a plane. Two Imager Pro X 4M LaVision CCD cameras with a resolution of 2042×2042 pixels were used to record images of the particles using a sampling rate such that there were 32 images per oscillatory period; the imaging frequency was set to 1.59 and 2.83 Hz for $\theta = 20.3°$ and $38.2°$, respectively. A shutter time of $10 \, \mu$s was used to ensure clear images of the particles; a representative value for the image magnification was ~ 0.1 mm/pixel.

The configuration for these experiments had both cameras on one side facing the image plane from the front of the test-section (i.e. a 'forward-backward scattering' camera set-up), as illustrated in Fig. 2(b). The two cameras, having opposite viewing directions with a separation angle of $\sim 65°$, were positioned roughly 45 cm from the front face of the tank. A drawback of the 'forward-backward scattering' configuration is that the camera facing the incoming laser receives forward scattered light whereas the camera facing the opposite direction receives scattered light in the backward direction. This results in one camera receiving higher intensity level images than the other. In
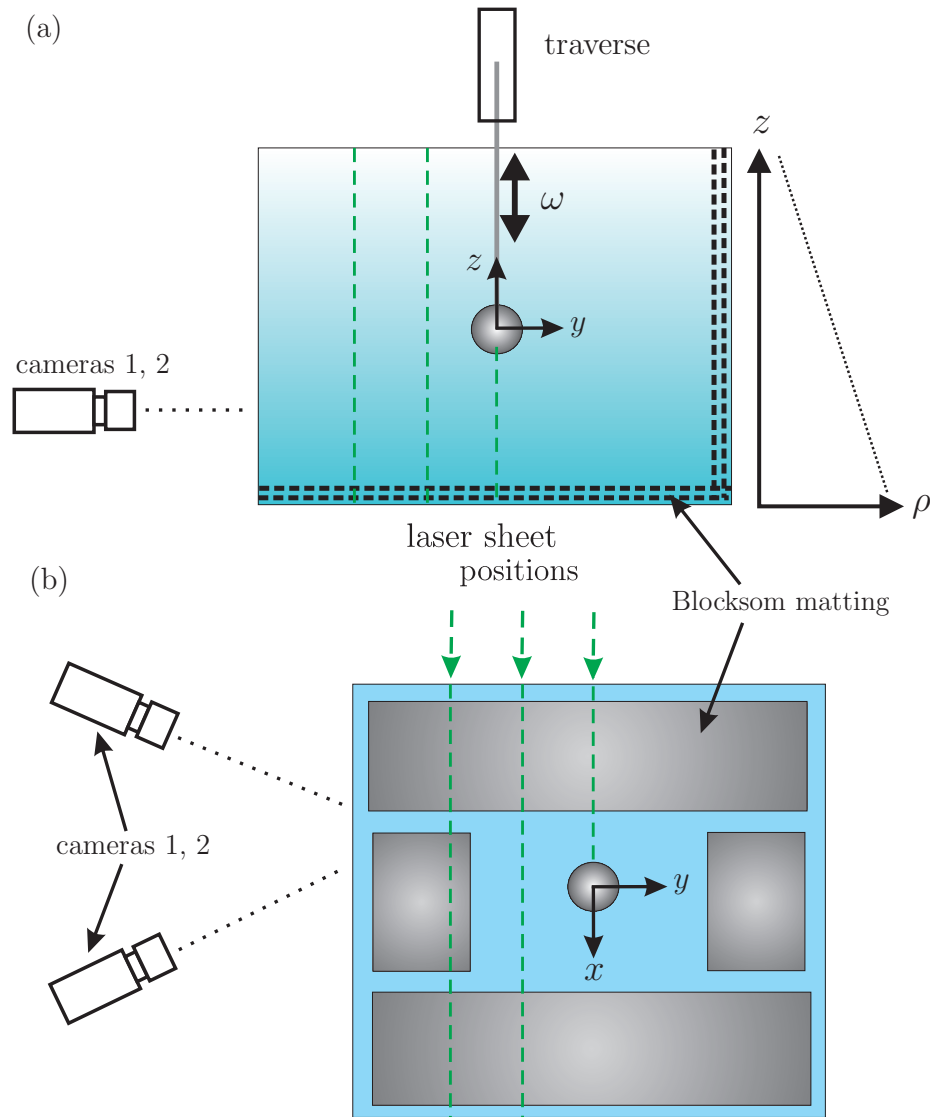
Fig. 2 Schematic of the experimental arrangement: (a) side view, (b) overhead view. The field of view encompassed the quadrant $x, z < 0$, along the cross-sectional planes $y = 0$ cm, -4 cm and -8 cm.

order to equalize the images collected from both cameras the aperture of the camera receiving backward scatter was larger.

A set of Scheimpflug adapters was attached to the cameras and adjusted so that the image, camera and object planes met at an intersection point some distance away in the direction opposite of the camera viewing, thus fulfilling the Scheimpflug criterion (Scheimpflug, 1904). To remedy the variable magnification of the two images obtained by the different cameras we used a two-level calibration plate and the commercial software package LaVision DaVis 7.2 to perform necessary calibration procedures.

Following the initial calibration procedure was the self-calibration process, which corrected for misalignment errors. Ideally, during the calibration procedure, the calibration plate is placed directly in the plane of the laser sheet. However, exact alignment is not possible, thus the mapping functions need to be modified to coincide with the plane of the laser sheet and not that of the calibration plate. To account for the potential misalignment, a self-calibration algorithm was used to modify the mapping functions found in the initial calibration procedure (as detailed in Wieneke (2005)). Once all particle images were mapped to a common reference frame centered on the laser sheet, a modified cross-correlation method was utilized in computing the (u, v, w) velocity fields. We used the DaVis 7.2 commercial stereoscopic PIV processing software package to perform the necessary stereoscopic reconstruction of the velocity fields.

A subtlety of stereoscopic PIV post-processing is the balance between having a large enough average particle displacement between image frames while maintaining a small enough time window so that the overall dynamics of the flow can be well-resolved. Given that the out-of-plane velocity component calculation is more sensitive to particle displacements between processed images in comparison to the in-plane velocity, we used a staggered processing approach. To facilitate this procedure we collected 32 images per period of oscillation so that the appropriate number of images (typically three) could be skipped in processing. We then repeated the velocity field calculation for every image obtained, thus maintaining the original resolution in time.

An important consideration for PIV studies of stratified flows is that changes in the density field due to internal wave activity correspond to changes in the refractive index field, which in turn affects the accuracy of the position and velocity measurements. The scale of these errors can be reasonably estimated following the work of Dalziel et al. (2007). Given that the fluid density varied by ~ 8 kg/m^3 over the ~ 15 cm tall visualization window, and that the smallest length scales in the excited wave cones are on the order of 1 cm, a reasonable upper bound for the horizontal and vertical density gradients induced by the wave field (which far exceed the modest background stratification) is $\nabla\rho \sim O(10^2)$ kg/m^4. The linear relation between refractive index and density for salt water (e.g. see equation 4, Dalziel et al. (2007)) correspondingly gives $\nabla n \sim O(10^{-2})$ 1/m. A relative order of magnitude estimate of the velocity measurement errors is then obtained using:

$$\Delta \boldsymbol{u} = \frac{1}{8} \frac{L^2}{n_o} \frac{\partial}{\partial t} \nabla n, \qquad (10)$$

where $L \sim O(10^{-1})$ m is the characteristic length scale traversed by a light ray within the experimental tank, $n_o \sim O(1)$ is the nominal refractive index of the working fluid and $\partial_t \nabla n \sim O(10^{-3})$ 1/ms for our wave fields with oscillation periods on the order of 10 seconds. Substituting these quantities into Eq. 10 yields velocity errors that are $O(10^{-6})$ m/s, which is three orders of magnitude smaller than the $O(10^{-3})$ m/s flow velocities observed in the experiment, and can therefore be considered negligible. Using the same scaling arguments, the error in the apparent position of a velocity measurement, $O(10^{-5})$ m, is also found to be negligible compared to the size of the experimental domain and can therefore be neglected.

In concluding, it should be furthermore noted that these upper bounds for errors in the velocity and position measurements are likely significant overestimates, since they are based on a model that assumes a light ray experiences the maximum refractive index gradient for the entirety of the optical path length L it traverses within the working fluid. In fact, a light ray traversing through the wave cone generated by an oscillating
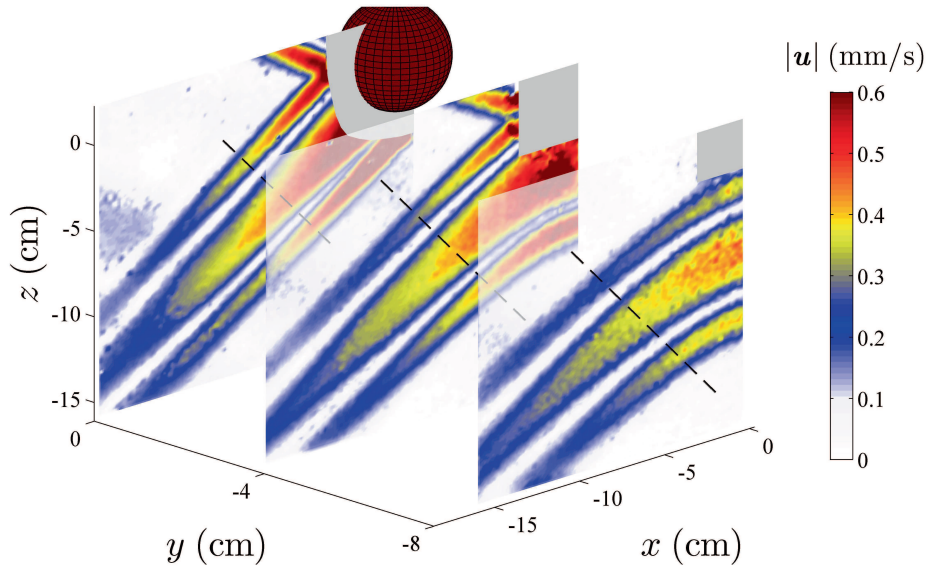
Fig. 3 Stereoscopic PIV visualization of the conical wave field for $\theta = 38.2°$; the colorbar is the total velocity $|\boldsymbol{u}| = \sqrt{u^2 + v^2 + w^2}$. Regions where experimental data were not reliable are shaded grey. The dashed lines indicate transects along which velocity profile data was analyzed. Note that the y-axis has been stretched for enhanced clarity.

sphere will only experience the maximum refractive index gradient for a short section of its optical path and will more typically experience much (i.e. an order of magnitude) weaker refractive index gradients characteristic of the background stratification.

5 Results

5.1 Linear wave field

The experimental results for the general structure of the wave cone radiated by the oscillating sphere for the $\theta = 38.2°$ case are presented in Fig. 3. The downward propagating wave cone is clearly visible with the curvature in the off center planes arising as a result of the conical structure of the wave beams. As expected, the velocity magnitude of the wave cone decreases with growing radial distance from the sphere center due to the combination of viscous dissipation and geometric spreading. The incongruity of the wave fields in the vicinity of the origin $(x, z) = (0, 0)$ in the off center cross-sectional planes is attributed to the close proximity of the laser sheet to the sphere, which obscured visualization particles in that corner of the field of view. Measurements presented in this sections were collected once the system was in a steady time-periodic state; nine periods was a sufficient amount of time for transients to fade away.

The across-beam velocity profiles for the transect in the $y = 0$ cm cross-sectional plane indicated in Fig. 3 are presented in Fig. 4; representative instantaneous profiles are used since negligible variability was observed over the steady-state wave periods. The in-plane velocities, u and w, exhibit fine agreement with the theoretical predictions detailed in section 2. Theory underpredicts the peak velocity amplitude in some cases
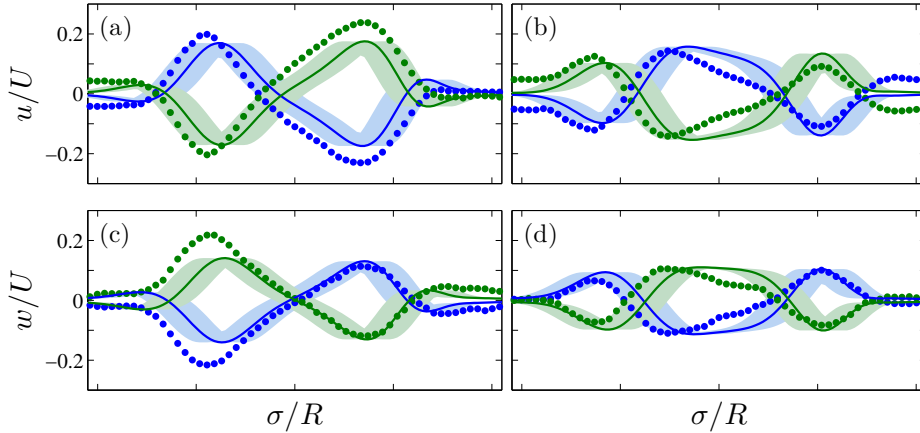
Fig. 4 Across-beam profiles of the $\theta = 38.2°$ wave field taken at $y = 0$ cm for u (top row) and w (bottom row). The profiles cover $\sigma = [-7, 7]$ cm and are located at $s = 10$ cm (see Fig. 3). The theoretical solution is plotted as a solid line (with the error due to inevitable small uncertainties in the experimental parameters represented by the lightly shaded area) and the experimental results are shown by the discrete points. Each panel contains profiles with a phase difference of $\Delta\Phi = \pi/\omega$; (a) and (c) are $\Phi = \pi/2\omega$ apart from (b) and (d). The velocity profiles have been normalized with respect to the max excitation velocity $U = A\omega$.

by about 25%, as can be seen in Figs. 4(a) and (c), and one possible source of this discrepancy is that theory does not fully account for the no-slip boundary condition on the surface of the oscillating sphere. The high degree of symmetry for the results separated by a π/ω phase lag is as one would expect for a linear wave field. A further testimony to the quality of the results is that we were unable to detect any discernable out-of-plane (i.e. v) velocity component, as one would expect in the mid-plane of the axisymmetric wave field generated by an oscillating sphere. We note that the relatively weak disagreement between the experimental results and theory could possibly be accounted for by the free-slip condition applied to the surface of the oscillating sphere in the theoretical formulation which stands in contrast to the viscous no-slip condition physically realized in the experiments.

Fig. 5 presents the across-beam profiles collected in the $y = -4$ cm cross-sectional plane. For this plane there is a significant out-of-plane velocity, v, that is detected by the stereoscopic PIV method. Again, there is overall very good agreement between experiment and theory, now for all three velocity components. Most strikingly, the v velocity component shows nearly perfect agreement with theory (Figs. 5(c) and (d)). The out-of-plane velocities are observed to be 50% weaker than the in-plane velocities, which is due to the close proximity of the observation plane to the sphere; at this location it is expected that the wave field be dominated by in-plane motion.

In Fig. 6, the results for the across-beam profiles collected in the $y = -8$ cm plane are presented. The agreement between experiment and theory is particularly good for v and w. Since the plane of reference is further away from the central plane of the sphere, the out-of-plane velocity component is comparable in magnitude to both of the in-plane components.
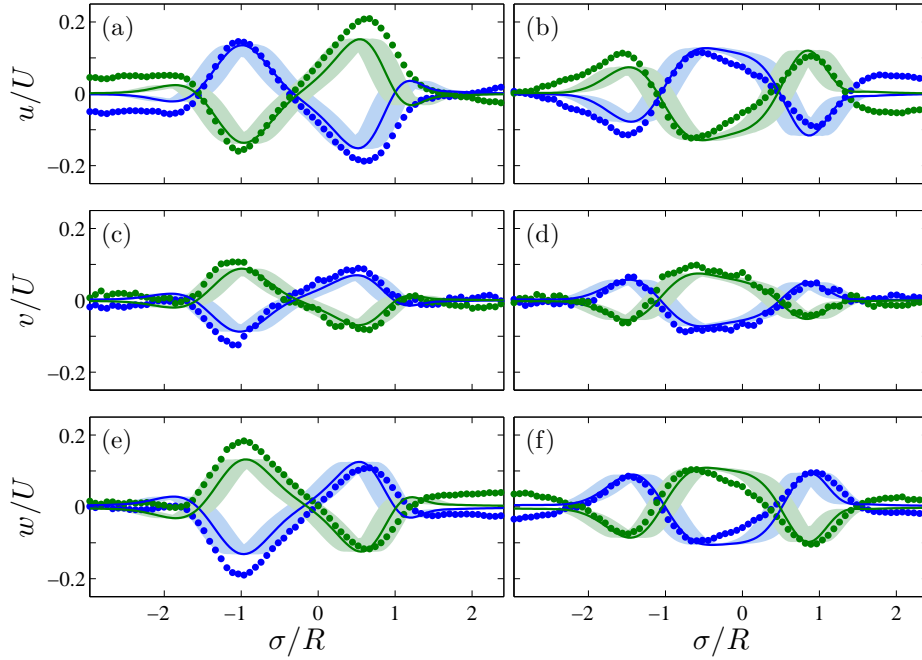
Fig. 5 Across-beam profiles of the $\theta = 38.2°$ wave field taken at $y = -4$ cm for u (top row), v (middle row) and w (bottom row). The profiles cover $\sigma = [-8, 6.5]$ cm and are located at $s = 10$ cm (see Fig. 3). The theoretical solution is plotted as a solid line (with the error due to inevitable small uncertainties in the experimental parameters represented by the lightly shaded area) and the experimental results are shown by the discrete points. Each panel contains profiles with a phase difference of $\Delta\Phi = \pi/\omega$; (a), (c) and (e) are $\Phi = \pi/2\omega$ apart from (b), (d) and (f). The velocity profiles have been normalized with respect to the max excitation velocity $U = A\omega$.

5.2 Nonlinear phenomena

Studies were also performed for an oscillation frequency such that the first harmonic wave cone propagation angle was $\theta = 20.3°$. A set of experimental results for this scenario is presented in Fig. 7. Comparisons of across-beam velocity profiles were made with theory for three different planes and the level of agreement was just as good as that observed for the $\theta = 38.2°$ wave field. A notable feature of the data presented in Fig. 7, however, is the existence of second harmonics propagating at an angle $\theta_2 = \sin^{-1}(2\omega/N) = 43.9°$. This feature of the wave field was generated by nonlinear processes in the immediate vicinity of the oscillating sphere. Ermanyuk et al. (2011) recently studied this nonlinear aspect of the generation process, highlighting how the amplitude of the vertical velocity field for the second harmonic could exceed that of the fundamental (first harmonic) forcing frequency. The authors provided a comprehensive investigation of this effect as a function of the amplitude of oscillation of the sphere.

An interesting aspect of the study of Ermanyuk et al. (2011) is that their experimental dye line investigations were only capable of detecting the vertical velocity component of the conical internal wave field. This naturally enhances the signal of the second harmonic compared to the first, since the dominant velocity component in a wave cone is along the direction of the cone angle and higher harmonic waves propagate
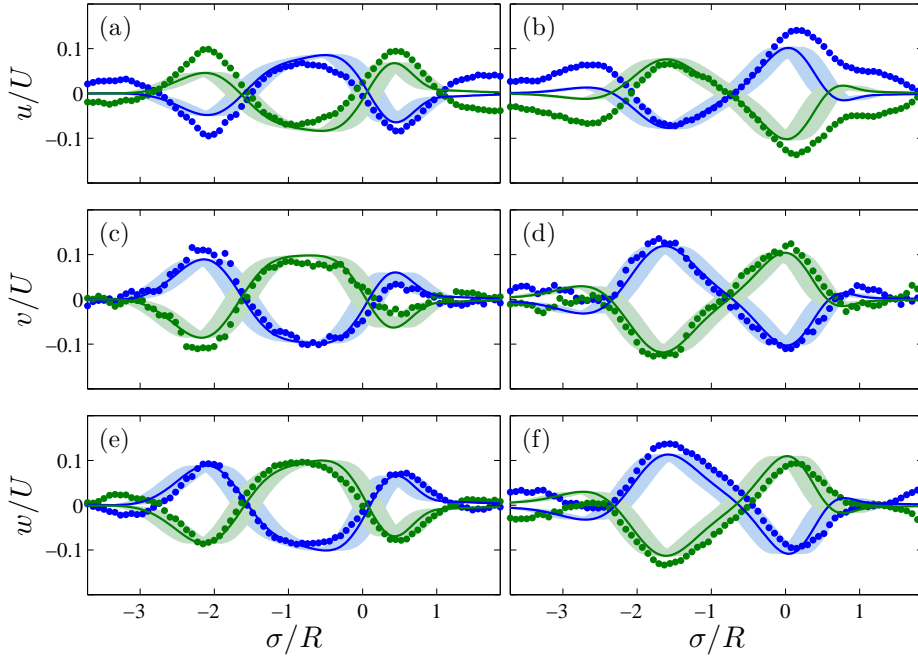
Fig. 6 Across-beam profiles of the $\theta = 38.2°$ wave field taken at $y = -8$ cm for u (top row), v (middle row) and w (bottom row). The profiles cover $\sigma = [-10, 5]$ cm and are located at $s = 10$ cm (see Fig. 3). The theoretical solution is plotted as a solid line (with the error due to inevitable small uncertainties in the experimental parameters represented by the lightly shaded area) and the experimental results are shown by the discrete points. Each panel contains profiles with a phase difference of $\Delta\Phi = \pi/\omega$; (a), (c) and (e) are $\Phi = \pi/2\omega$ apart from (b), (d) and (f). The velocity profiles have been normalized with respect to the max excitation velocity $U = A\omega$.

within steeper wave cones. Furthermore, Ermanyuk et al. (2011) investigated the wave field along horizontal transects at several different vertical locations. To reach such transects, first harmonic waves must travel radially farther than second harmonics and are therefore subject to more substantial geometric spreading and viscous damping. Overall, therefore, the investigations of Ermanyuk et al. (2011), while not being incorrect, were inherently predisposed to a natural augmentation of the second harmonic signal compared to the first harmonic. Using stereoscopic PIV, however, we have access to all velocity components along any transect in a vertical plane.

To investigate the relative strengths of the first and second harmonics, we considered the total velocity $|\boldsymbol{u}|$ along the transects illustrated in Fig. 7, which are oriented at a mean angle $\bar{\theta} = (\theta_1 + \theta_2)/2$ between the first and second harmonic wave cones. By analyzing the total velocity along these across-beam transects we do not bias the results in favor of either the first or second harmonic. We note that the Keulegan-Carpenter number, $Ke = A/R$, for our studies ($Ke = 0.19$) lay within the range investigated by Ermanyuk et al. (2011) ($0.13 \leq Ke \leq 0.27$). In Fig. 8 we present the results of the harmonic analysis of the total velocity $|\boldsymbol{u}|$ along these transects. As a consequence of our different perspective, we reveal the second harmonic to actually be an order of magnitude weaker than the first harmonic for all the transects in all cases, with the exception of a small portion of the $y = 0$ cm transect that contains the second
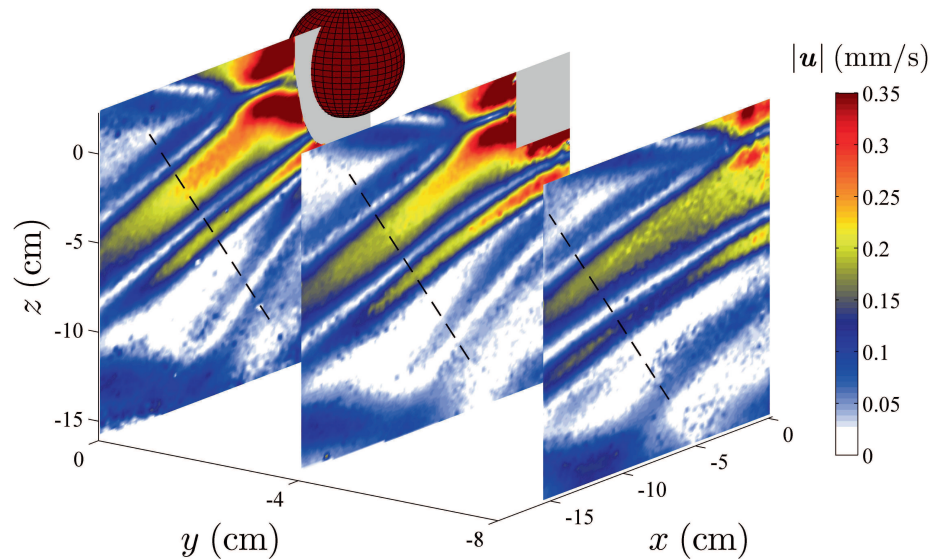
Fig. 7 Stereoscopic PIV visualization of the conical wave field for $\theta = 20.3°$; the colorbar is the total velocity $|\boldsymbol{u}| = \sqrt{u^2 + v^2 + w^2}$. Regions where experimental data were not reliable are shaded grey. The transects are located at $s = 13$ cm and cover $\sigma = [-8, 8]$ cm. Note that the y-axis has been stretched for enhanced clarity.

harmonic wave cone, where we find the first and second harmonics to be of the same order.

6 Conclusion

In conclusion, we have performed the first laboratory experimental investigation of a three-dimensional internal wave field using stereoscopic PIV. The experiments used the canonical arrangement of a vertically oscillating sphere in a uniform density stratification. Direct comparisons were made between experimental data and the predictions of the recent theoretical model of Voisin et al. (2011) for all three velocity components in three different cross-sectional planes of the wave field. The level of agreement between experiment and theory was generally excellent, particularly for the out-of-plane velocity component, and comparable to the level of agreement obtained using planar PIV (King et al., 2009) and dye layer (Ermanyuk et al., 2011) methods. The advantage of using stereoscopic PIV compared to the other two methods is having access to all three velocity components. By so doing, we were able to provide an alternative perspective to Ermanyuk et al. (2011) on the strength of second harmonic relative to first harmonic waves, the former being created by nonlinear processes in the vicinity of the oscillating sphere.

References

J. C. Appleby and D. G. Crighton. Internal gravity waves generated by oscillations of a sphere. *J Fluid Mech*, 183:439–450, 1987.
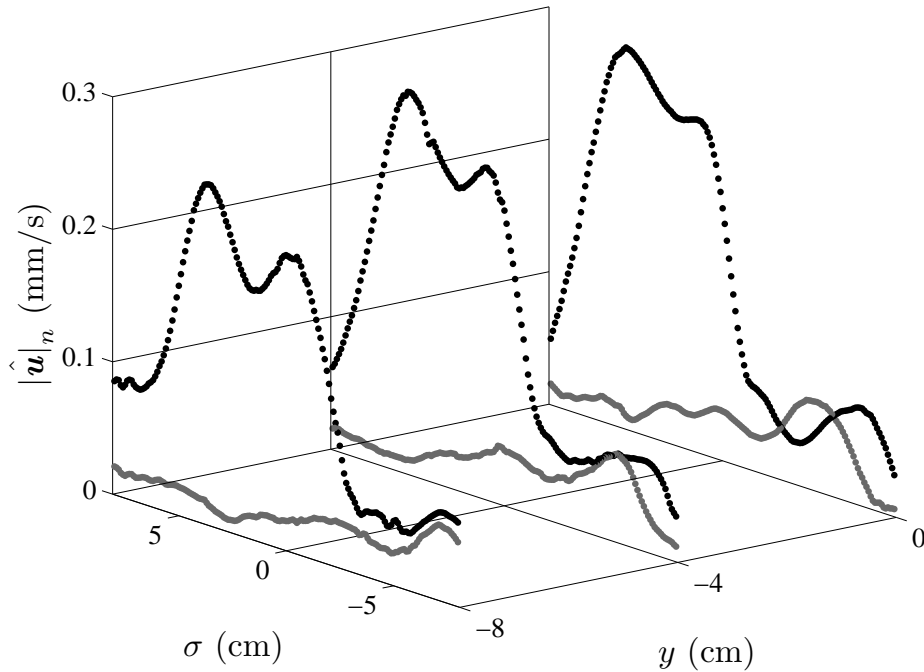
Fig. 8 Profiles for the $\theta = 20.3°$ wave field displaying the first harmonic (black dots) and second harmonic (grey dots) content of the total velocity $|\boldsymbol{u}| = \sqrt{u^2 + v^2 + w^2}$ along the transects shown in Fig. 7.

S. B. Dalziel, M. Carr, J. K. Sveen, and P. A. Davies. Simultaneous synthetic schlieren and PIV measurements for internal solitary waves. *Meas Sci Technol*, 18:533–547, 2007.

P. Echeverri, M. R. Flynn, K. B. Winters, and T. Peacock. Low-mode internal tide generation by topography: an experimental and numerical investigation. *J Fluid Mech*, 636:91–108, 2009.

E. V. Ermanyuk, J.-B. Flor, and B. Voisin. Spatial structure of first and higher harmonic internal waves from a horizontally oscillating sphere. *J Fluid Mech*, 671: 364–383, 2011.

M. R. Flynn, K. Onu, and B. R. Sutherland. Internal wave excitation by a vertically oscillating sphere. *J Fluid Mech*, 494:65–93, 2003.

C. Garrett and E. Kunze. Internal tide generation in the deep ocean. *Ann. Rev. Fluid Mech.*, 39:57–87, 2007.

V. H. Gortler. Uber eine Schwingungserscheinung in Flussigkeiten. *Zeitschrift fur angewandte mathematik und mechanik*, 23:65–71, 1943.

J. Hazewinkel, L. R. M. Maas, and S. B. Dalziel. Tomographic reconstruction of internal wave patterns in a paraboloid. *Exp Fluids*, 50:247–258, 2011.

D. G. Hurley. A general method for solving steady-state internal gravity wave problems. *J Fluid Mech*, 56:721–740, 1972.

B. King, H. P. Zhang, and H. L. Swinney. Tidal flow over three-dimensional topography in a stratified fluid. *Phys Fluids*, 21:116601, 2009.

M. J. Lighthill. *Waves in fluids*. Cambridge University Press, 1978.

M. Mathur and T. Peacock. Internal wave beam propagation in non-uniform stratifications. *J Fluid Mech*, 639:133–152, 2009.

M. J. Mercier, N. B. Garnier, and T. Dauxois. Reflection and diffraction of internal waves analyzed with the Hilbert transform. *Phys Fluids*, 20:086601, 2008.

D. E. Mowbray. The use of schlieren and shadowgraph techniques in the study of flow patterns in density stratified liquids. *J Fluid Mech*, 27:595–608, 1967.

D. E. Mowbray and B. S. H. Rarity. A theoretical and experimental investigation of the phase configuration of internal waves of small amplitude in a density stratified liquid. *J Fluid Mech*, 28:1–16, 1967.

G. Oster and M. Yamamoto. Density gradient techniques. *Chem Rev*, 63(3):257–268, 1963.

T. Peacock, P. Echeverri, and N. J. Balmforth. An experimental investigation of internal tide generation by two-dimensional topography. *J Phys Oceanogr*, 38:235–242, 2008.

T. Scheimpflug. Method of distorting plane images by means of lenses or mirrors. Patent No. 751347, February 1904.

B. R. Sutherland, S. B. Dalziel, G. O. Hughes, and P. F. Linden. Visualization and measurement of internal waves by 'synthetic schlieren'. Part 1. Vertically oscillating cylinder. *J Fluid Mech*, 390:93–126, 1999.

B. R. Sutherland and P. F. Linden. Internal wave excitation by a vertically oscillating elliptical cylinder. *Phys Fluids*, 14:721–731, 2002.

N. H. Thomas and T. N. Stevenson. A similarity solution for viscous internal waves. *J Fluid Mech*, 54:495–506, 1972.

B. Voisin. Limit states of internal wave beams. *J Fluid Mech*, 496:243–293, 2003.

B. Voisin, E. V. Ermanyuk, and J.-B. Flor. Internal wave generation by oscillation of a sphere, with application to internal tides. *J Fluid Mech*, 666:308–357, 2011.

B. Wieneke. Stereo-PIV using self-calibration on particle images. *Exp Fluids*, 39:267–280, 2005.

K. Y. Yick, C. R. Torres, T. Peacock, and R. Stocker. Enhanced drag of a sphere settling in a stratified fluid at small Reynolds numbers. *J Fluid Mech*, 632:49–68, 2009.

H. P. Zhang, B. King, and H. L. Swinney. Experimental study of internal gravity waves generated by supercritical topography. *Phys Fluids*, 19:096602, 2007.